ADVANCED ELECTRONIC MATERIALS Open Access
www.advelectronicmat.de

ZrNb(CO) RF Superconducting Thin Film with High Critical Temperature in the Theoretical Limit

Zeming Sun, Thomas Oseroff,* Zhaslan Baraissov, Darrah K. Dare, Katrina Howard, Benjamin Francis, Ajinkya C. Hire, Nathan Sitaraman, Tomas A. Arias, Mark K. Transtrum, Richard Hennig, Michael O. Thompson, David A. Muller, and Matthias U. Liepe**

Superconducting radio-frequency (SRF) resonators are critical components for particle accelerator applications, such as free-electron lasers, and for emerging technologies in quantum computing. Developing advanced materials and their deposition processes to produce RF superconductors that yield nΩ surface resistances is a key metric for the wider adoption of SRF technology. Here, ZrNb(CO) RF superconducting films with high critical temperatures (T_c) achieved for the first time under ambient pressure are reported. The attainment of a T_c near the theoretical limit for this material without applied pressure is promising for its use in practical applications. A range of T_c, likely arising from Zr doping variation, may allow a tunable superconducting coherence length that lowers the sensitivity to material defects when an ultra-low surface resistance is required. The ZrNb(CO) films are synthesized using a low-temperature (100 – 200 °C) electrochemical recipe combined with thermal annealing. The phase transformation as a function of annealing temperature and time is optimized by the evaporated Zr-Nb diffusion couples. Through phase control, one avoids hexagonal Zr phases that are equilibrium-stable but degrade T_c. X-ray and electron diffraction combined with photoelectron spectroscopy reveal a system containing cubic β-ZrNb mixed with rocksalt NbC and low-dielectric-loss ZrO_2. Proof-of-concept RF performance of ZrNb(CO) on an SRF sample test system is demonstrated. BCS resistance trends lower than reference Nb, while quench fields occur at approximately 35 mT. The results demonstrate the potential of ZrNb(CO) thin films for particle accelerators and other SRF applications.

1. Introduction

Superconducting radio-frequency (SRF) resonators are critical components for particle accelerator applications, including synchrotrons and free-electron lasers (the fourth-generation light source),[1–5] high-energy particle colliders,[6] nuclear physics experiments,[7] dark-matter detection,[8] materials/chemistry/biology research,[3,9,10] and medical/biopharmaceutic applications,[10] alongside technologies in < 5 nm semiconductor device fabrication[11] and quantum computing.[12–14] SRF resonant devices, such as SRF accelerating cavities and superconducting quantum qubits (**Figure 1**a), require low-temperature RF superconductors owing to their excellent superconducting and material properties that facilitate technology transfer to practical applications.[15]

RF superconductors such as Nb, Nb_3Sn, NbN, NbTiN, NbTi, NbSi, NbRe, V_3Si, etc., although studied decades ago, have been revitalized when tailored to emerging SRF applications.[23–27] These low-temperature superconductors can achieve ultra-low RF resistances

Z. Sun, T. Oseroff, K. Howard, M. U. Liepe
Cornell Laboratory for Accelerator-Based Sciences and Education
Cornell University
153 Sciences Drive, Ithaca, NY 14853, USA
E-mail: zs253@cornell.edu; teo26@cornell.edu; mul2@cornell.edu

The ORCID identification number(s) for the author(s) of this article can be found under https://doi.org/10.1002/aelm.202300151

DOI: 10.1002/aelm.202300151

Z. Baraissov, D. A. Muller
School of Applied and Engineering Physics
Cornell University
142 Sciences Drive, Ithaca, NY 14853, USA

D. K. Dare
Cornell Center for Materials Research
Cornell University
627 Clark Hall of Science, Ithaca, NY 14853, USA

B. Francis, M. K. Transtrum
Department of Physics & Astronomy
Brigham Young University
N283 Eyring Science Center, Provo, UT 84602, USA

A. C. Hire, R. Hennig
Department of Materials Science and Engineering
University of Florida
100 Rhines Hall, Gainesville, FL 32611, USA

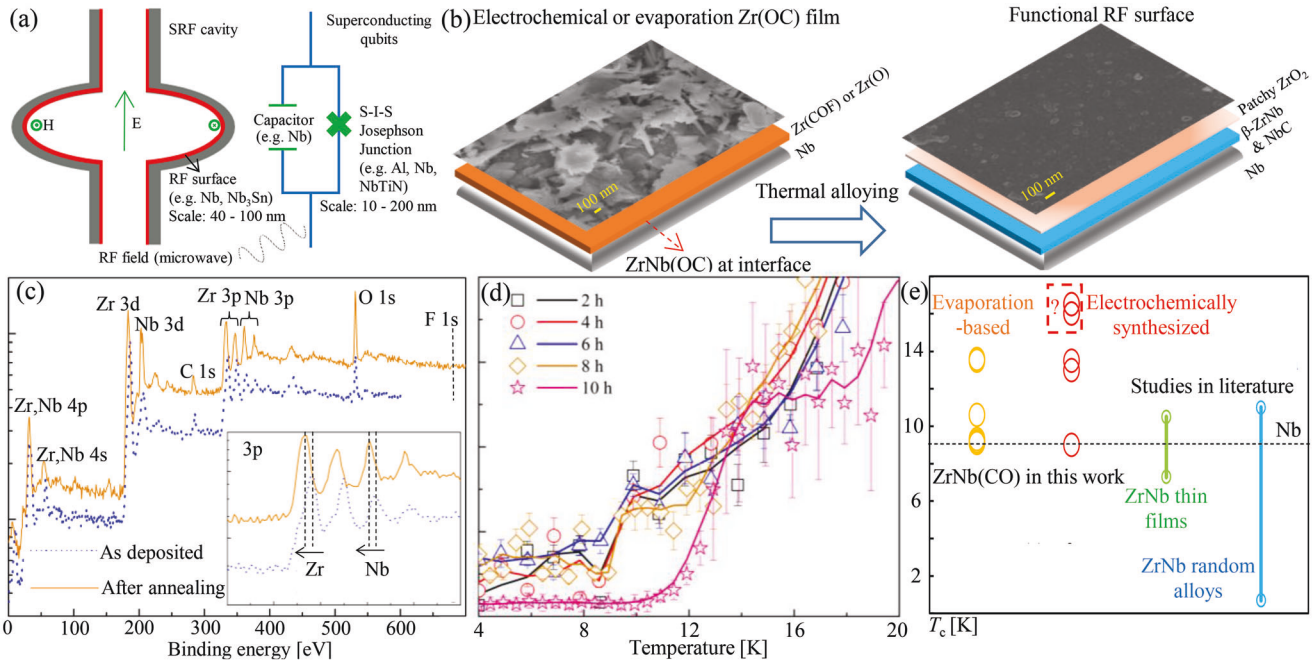

Figure 1. ZrNb(CO) alloying via electrochemical synthesis and thermal annealing to enable functional SRF surfaces. a) SRF cavity and quantum computing qubit, showing the use of SRF thin films. b) Schematic showing the alloying process and surface morphology. c) XPS spectra taken after removing surface oxides on samples as-deposited versus thermally annealed. d) Resistivity drop measurements to determine T_c for electrochemical samples made via 2 –10 h synthesis followed by annealing, with a note on the potential impact of wire bonding on measurements for 2 – 8 h deposited nanometer-thin films. e) T_c comparison between the electrochemical ZrNb(CO) and evaporated Zr-Nb diffusion couples with experimental results from literature.[16–22]

(nΩ-scale) in the vortex-free state. The active surface layer of SRF cavities or quantum qubits with excited RF fields has a depth of tens of nanometers, for example, 40 nm for conventional Nb (dictated by field penetration depth). Here, we aim to engineer a thin ZrNb(CO) film through electrochemical synthesis and post-processing to obtain the desired phase and composition, yielding a combination of superconducting parameters suitable for RF applications, particularly SRF cavities.

Since the adoption of superconducting technology, RF cavities are reliant on bulk Nb, for example, for Linac Coherent Light Source II. However, Nb cavities, with a superheating field of 200 mT and critical temperature (T_c) of 9.2 K, are reaching the theoretical limits of ≈ 50 MV m^{-1} accelerating gradients and (4 – 6) × 10^{10} quality factors at 2 K, 1.3 GHz operations.[28] A quantum leap in SRF R&D, involving high beam energy, high accelerating gradient, compact size, and low cost, requires searching for new SRF materials, with three primary goals:

- Increasing T_c to lower the cost and complexity of cryogenic systems while maintaining RF performance;
- Reducing surface resistance, R_s, and proportionally boosting quality factors, Q_0, which minimize the cost-driving power dissipation;
- Enhancing the accelerating gradient, E_{acc}, which is limited by the intrinsic superheating field, B_{sh}, of the superconductor.

Currently, Nb_3Sn is a strong candidate owing to its high predicted B_{sh} of ≈ 400 mT (corresponding to ≈ 100 MV m^{-1} E_{acc}) and high T_c of 18 K, allowing cost-effective 4.2 K accelerator operations.[23] Nb_3Sn cavities have now been developed into full-scale 9-cell operations.[29] Other materials of interest, including NbN,[24] NbTiN,[24–26] V_3Si,[27] and MgB_2,[24] are in the early R&D stage. To date, among these alternative SRF materials, only Nb_3Sn has reached the phase of the first technology transfer to accelerator products.[29] Still, current Nb_3Sn cavities suffer from the typical quench fields of 13 – 18 MV m^{-1} E_{acc} (with the highest value of 24 MV m^{-1}[29]), considerably lower than the predicted ultimate limit of ≈ 100 MV m^{-1}.[29] While ongoing atomic[30] and theoretical[31] analyses combined with the growth optimization of Nb_3Sn films[32] continue, further efforts are called for to seek alternative materials and surface structures.

Our motivation for exploring ZrNb alloying stems from several fundamental aspects. Recently, theorists within the Center for Bright Beams have discovered the exciting potential of ZrNb alloys for SRF, predicting high T_c's up to 17.7 K and high B_{sh}'s up to 350 mT.[33,34] These large values promise similar benefits as Nb_3Sn. Moreover, the ability to tune the Zr concentration profile in ZrNb allows for manipulation of T_c and coherence length (ξ), which can reduce sensitivity to defects.[35] In contrast, Nb_3Sn has a small ξ of 3 nm resulting in strong sensitivity to material

N. Sitaraman, T. A. Arias
Department of Physics
Cornell University
109 Clark Hall, Ithaca, NY 14853, USA
M. O. Thompson
Department of Materials Science and Engineering
Cornell University
210 Bard Hall, Ithaca, NY 14853, USA

disorders, which is likely one of the limiting factors in reaching its theoretical performance. This experimental work, stimulated by the theoretical predictions,[33,34] intends to achieve Zr substitutional doping in the Nb bcc lattice to increase T_c compared to Nb while maintaining reasonably large B_{sh}'s and ξ's, minimizing defect sensitivity, and facilitating the realization of enhanced cavity performance.

ZrNb random alloys, usually made by atmospheric arc, induction, or levitation melting, have been studied since the 1960s.[16–18] These Zr-rich (> 80 %) alloys are mainly used for magnet construction,[16] nuclear structure,[36–41] and biomedical[42] applications. As for superconducting applications, prior to this work, the highest T_c obtained was 11 K,[16–18] lower than the predicted 17.7 K T_c value[33] in an ordered, cubic (β) structure.

Phase transformations are the dominant factor preventing ZrNb T_c from reaching the predicted maximum. Theoretical analysis indicates that locking the bcc β phase that is not an equilibrium-stable phase is the route to obtaining a high T_c of 17.7 K in ZrNb.[33] This prediction is supported by T_c values measured under extreme conditions, for example, at 2.8×10^5 atmospheric pressure.[43] Additionally, simulations on β-Zr obtained at 30 GPa pressure show a high T_c of 17.1 K, whereas the complexity of Zr phase transformations in experiments results in a 10 K T_c at the same pressure.[44] Our goal is to produce a stable β-ZrNb phase at room temperature and atmospheric pressure, thus translating theoretical predictions into practical SRF applications.

High-temperature ZrNb solid solutions exist in the bcc β phase (phase diagram[45]) while interdiffusion coefficients are high, for example, 10^5 nm^2 s^{-1} for Nb into pure Zr and vice versa 10^{-1} nm^2 s^{-1} at 1000 ° C.[46] However, the equilibrium-stable phase at room temperature is the hcp α-Zr phase with a low T_c of 7 K.[16,44] Moreover, the metastable hcp ω phase with a 4 K T_c[44] frequently appears through quenching from above 1000 ° C temperatures (diffusionless $\beta \rightarrow \omega$), although the majority β phase is frozen, or through 350 – 850 ° C low-temperature aging, that is, $\beta \rightarrow (\beta + \omega) \rightarrow (\beta + \alpha)$.[47,48] Additionally, martensite α'-Zr is observed through rapid quenching (for example, water cooling) in Zr-rich alloys, but it evolves into β and α upon post-annealing, for example, at 600 ° C.[36,39,40,42,49] The α'-Zr phase is treated as an athermal ω phase by some researchers,[48] but their reported diffraction angles differ.[36,42,49]

Table S1 (Supporting Information) summarizes the phase transformations, heat treatments, and composition ranges for ZrNb random alloys reported in the literature.[16–18,36–42,49,50] Clearly, the α, ω, and α' phases are difficult to avoid in random alloys. For the conditions observing β phases, one should be cautious about the limitation of phase determination techniques, especially concerning the low T_c's obtained. Moreover, phase separation is typical in the form of α-Zr and β-Nb precipitates at grain boundaries.[16,36,40,49] A single β-ZrNb phase is possible, as indicated by the shift of diffraction peaks in few studies.[42] Instead of these well-studied random alloys, we adopt an electrochemical surface alloying process that leverages the unique reaction between Zr precursors and the parent bcc-Nb surface to achieve a substitutional bcc system, as illustrated in Figure 1b.

Thin-film ZrNb has been produced by co-sputtering, yielding a T_c of 9.1 K.[19] The thickness modulation of thin Zr and Nb layers can enhance their T_c values to 10.5 K.[20–22] This enhancement is induced by the proximity effect, which maintains a high T_c if the dimension of low-T_c or even normal-conducting phases is smaller than the coherence length. Furthermore, phase stability studies show that bcc Zr is greatly favored over hcp Zr, owing to the smaller interfacial energy, as the dimension of Zr phases is reduced and the Nb fraction is increased for films with over 50 at.% Nb.[51] Also, the improvement of bcc-ZrNb stabilization is observed in simulations of Nb-rich bulk alloys.[52] Hence, our synthesis of inhomogeneous compositions with > 50% Nb fractions provides flexibility in uniformity while facilitating bcc phase control and achieving suitably high T_c's. (Note that the superheating field is not affected by this inhomogeneous design.[34])

Our electrochemical method meets the multi-scale needs ranging from deposition at the inner surface of a meter-long, complicated SRF cavity to the fabrication of nanoscale quantum devices. Previous investigations on Zr electrochemical deposition mainly focused on high-temperature (500 – 850 ° C) eutectic salts, as summarized in Table S2 (Supporting Information).[53–64] However, these high temperatures are not practical for regular operations in an inert-gas glovebox, along with our concern of impurity doping induced.[65] Indeed, low-temperature attempts are still missing. Moreover, chloride and chloride-fluoride studies suggest multiple reduction steps, unfortunately, prevail, for example, $Zr^{4+} \rightarrow Zr^{2+} \rightarrow Zr$.[54,56,57,59,60,62] Therefore, we have developed a low-temperature (< 200 ° C) ionic-liquid process using fluorides that permit single-step reduction.

Here we present high-T_c ZrNb(CO) thin films produced using our electrochemical recipe, in combination with phase investigations using Zr-Nb diffusion couples. The inhomogeneous surface consisting of β-ZrNb and ZrO_2, mixed with rocksalt NbC in some samples, yields the highest-ever T_c values for this material system under ambient pressure. The highest values, as measured by temperature-dependent resistivity drops, are at least 13 K (Figure 1d; Figure S16, Supporting Information), with possible 16 K values indicated by flux expulsion tests (Figure S2 and uncertainty analyses in Supporting Information). Our phase control and post-processing address the equilibrium constraints from hexagonal formations, leading to high T_c values that were previously only observed in theoretical simulations and extreme conditions.

2. Results and Discussion

2.1. Zr Electrochemical Synthesis on Nb

We have developed a low-temperature (100 – 200 ° C) Zr electroplating process on the Nb surface (see Experimental Section). We optimized the solution chemistry, reduction potentials, deposition temperature, and time using cyclic voltammetry (CV) and potentiostat. The CVs (Figure S3, Supporting Information) exhibit two reduction potentials at around -1 and -2.8 V versus a Pt quasi-reference. By examining the deposits under scanning electron microscopy equipped with energy-dispersive X-ray spectroscopy (SEM/EDS) and X-ray photoelectron spectroscopy (XPS), we assigned the low reduction potential as Zr reduction and the high potential as electrolyte decomposition. The Zr

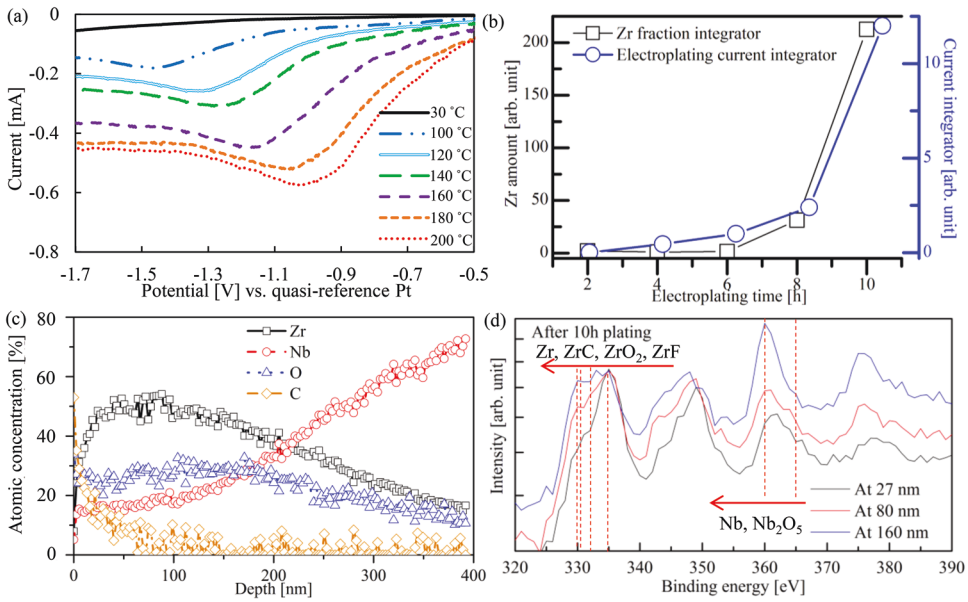

Figure 2. Electrochemical and physical analysis of Zr synthesis on Nb. a) Temperature-dependent CVs. b) Total Zr amount and the corresponding plating current integrated over time, showing explosive Zr growth with onset at around 8 h. c,d) XPS elemental profiles (Zr, Nb, O, C) and 3p spectra (Zr, Nb) as a function of depth for electrochemical deposits prepared via 10 h synthesis.

reduction potential depends on the Zr^{4+} concentration (following the Nernst equation) and the bath temperature that affects the Zr^{4+} dissolution. As shown in **Figure 2**a, the reduction shifts from - 1.5 to - 1 V at increasing temperatures, along with an enlarged plating current. At increasing plating time under potentiostat, we observe an explosive Zr growth mode along with dendrite formation. Quantifying the total amount of Zr, probed by XPS and indicated by the integral of the plating current over the synthesis time (Figure 2b), reveals rapid growth with an onset at around 8 h. Surface SEM images (Figure S4, Supporting Information) show the nucleation of Zr sites at 2 h and the formation of thin Zr films at 8 h. The dendrites and a large amount of Zr deposition appear at 10 h.

Elemental analysis of the deposits, for example, after 10 h of synthesis (Figure 2c,d), suggests that the alloying between Zr and Nb arises from reactive synthesis, generating the metallic Zr and Nb photoelectrons throughout the film, which matches the reactivity study.[66] Oxygen appears within the deposits, and carbon accumulates only at the surface region. EDS spectra (Figure S6a, Supporting Information) show fluorine impurities that are later removed during thermal annealing (Figure S6c, Supporting Information); this behavior is confirmed by XPS (Figure 1c).

The Zr and Nb 3p (Figure 2d) and 3d (Figure S7d, Supporting Information) photoelectrons at different depths of the film show peak shiftings toward metallic motifs at increasing depths. Surface motifs, for example, at a 27 nm depth, may include zirconium carbides, oxides, fluorides, and niobium oxides in addition to metallic zirconium and niobium. Upon thermal annealing (Figure 1c; Figure S5, Supporting Information), the Zr and Nb peaks further shift to the metallic motifs together with the formation of ZrO_2 and NbC. Since Zr typically shows strong gettering behaviors, we infer that impurity incorporation may not be fully avoided during synthesis, even under an inert-gas environment (O_2 and H_2O levels below 0.5 ppm). Instead of further resolving impurity control, we focus on analyzing the impurity-induced phases in the final products after thermal annealing (see next section).

2.2. Phase Transformation Mechanisms and High T_c

We first analyze the phase transformation after thermal annealing using evaporated Zr-Nb diffusion couples. Samples with initial Zr thicknesses of 20 – 40 nm, which readily oxidized after evaporation (Figure S14, Supporting Information), were annealed under a vacuum of 2×10^{-7} torr at temperatures of 600 and 1000 ° C for durations of 20 min to 10 h. X-ray diffraction (XRD) patterns in Figure S15 (Supporting Information) show the appearance of hcp α- and ω-Zr and ZrO_2, with indexing carefully referenced to the literature,[36,42,48,49,67] as summarized in Table S3 (Supporting Information). ω-Zr is hard to distinguish as its diffraction angles are close to some α- and β-Zr angles. After annealing, Zr doping peaks or shoulders appear on the lower 2θ regime next to the Nb peaks. Additionally, the Nb peaks slightly shift to lower 2θ values. Although we performed resistivity drop measurements using four probes on the surface of the annealed samples, we did not observe any T_c transition in the samples due to the presence of thick oxides on their surfaces.

After etching the oxidized surface using HF acid, as shown in **Figure 3**a, we notice the disappearance of hcp phases, regardless of α-Zr or possible ω-Zr. Moreover, the Zr doping peaks assigned to β-ZrNb become apparent, in addition to the Nb peak shifting. According to Bragg's and Vegard's laws, $\sin\theta \propto 1/a$ in a cubic system, and a is linearly dependent on c, where θ is the diffraction angle, a is the lattice parameter, and c is the doping concentration. The substitutional Zr doping in a cubic Nb structure induces the diffractions between bcc Nb and Zr angles. Note

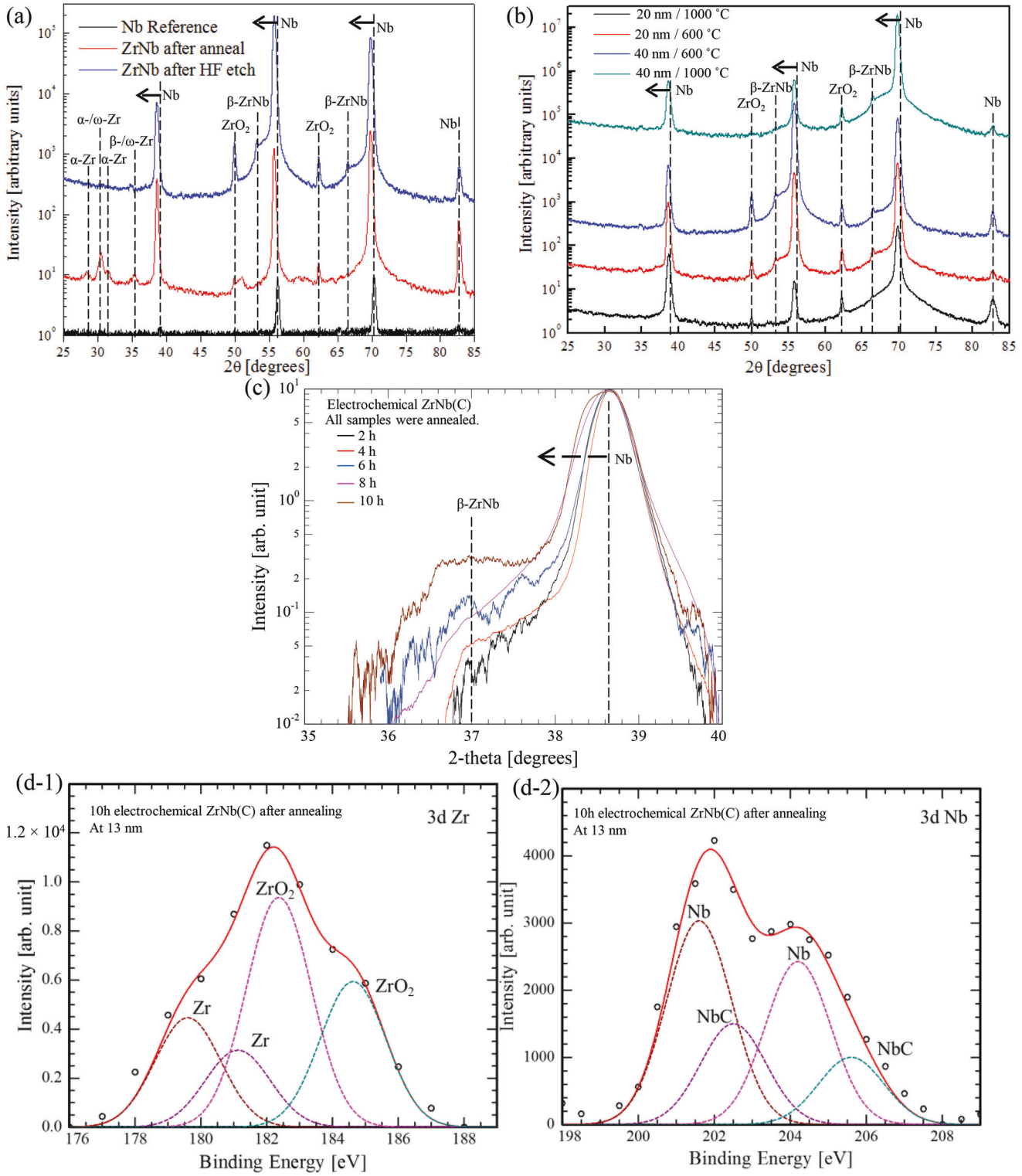

Figure 3. Phase analysis of Zr-Nb diffusion couples and electrochemically synthesized ZrNb(CO) after thermal annealing. a) Phase evolution of ZrNb diffusion couples after annealing at 600 ° C for 10 h and after HF etch, compared to the Nb reference. b) Phase comparison of ZrNb after annealing under different conditions for 10 h. These samples underwent HF etching. c) XRD patterns of the annealed ZrNb(CO) synthesized for varying times. d) Deconvolution of XPS 3d spectra (Zr, Nb) for ZrNb(CO) prepared by 10 h plating and annealed at 600 ° C for 10 h. Note that the spectra shifted to lower binding energies by 0.6 ± 0.1 eV caused by the use of the neutralizer.

that Zr's and Nb's bcc lattice parameters are 0.354 and 0.330 nm, respectively.[51] These β-ZrNb diffractions are repeated for different annealing conditions with hexagonal Zr phases eliminated (Figure 3b). As shown in Figure S16 (Supporting Information), the diffusion couples made from 10 h annealing followed by etching show T_c values ranging from 10.5 to 13.5 K. In contrast, the 20 min annealed samples show a niobium 9 K T_c upon etching, indicating excessive etching on these samples. We find that the low-temperature anneals at 600 ° C yield higher T_c values than the 1000 ° C anneals. At 1000 ° C (see phase diagram[45]), a thick region turns to a complete solid solution, and the subsequent cooling unalterably induces a large amount of α-Zr precipitates, which degrade the T_c. We, therefore, adopt the 600 ° C, 10 h condition for annealing the electrochemical samples.

The annealed electrochemical ZrNb(CO) films show grain sizes of approximately 10 – 20 nm (Figure S8, Supporting Information). XRD patterns of samples prepared from different synthesis times (Figure 3c) exhibit the β-ZrNb phase with Nb peaks slightly shifting toward lower diffraction angles after annealing. XPS results further confirm the ZrNb alloying with distinctive metallic motifs at low binding energies (Figure 3d). However, carbon and oxygen remain present (Figure S7b,c, Supporting Information), with oxygen existing throughout the film and carbon primarily appearing in the surface 20 nm region. Under 4D-STEM, rocksalt niobium carbide is identified, as shown in Figure S11 (Supporting Information). XPS also suggests the presence of NbC in the ZrNb film (Figure 3d-2). Oxygen is fully bonded to Zr, as evidenced by the distinctive oxide peaks at high XPS binding energies (for example, Figure 3d-1). Nb oxides at 207 – 210 eV are not observed (for example, Figure 3d-2), but Nb sub-oxides may exist. Pure ZrO_2 of 1 – 3 nm exists on all samples, as shown in Figure S10 (Supporting Information). This wide bandgap dielectric is a perfect choice for SRF applications. To sum up, we infer our electrochemical ZrNb(CO) includes β-ZrNb, NbC, and ZrO_2.

The T_c results obtained from the 10 h synthesis of electrochemical samples showed a value of 13 K, as measured by the resistivity drop on ≈ 1 cm^2 deposits (Figure 1d). In contrast, during the flux expulsion test on 127 cm^2 cavity-plate deposits, a small but consistent change in the magnetic field ($\approx$ 0.4 mG) was observed at approximately 16 K on three flux gates located at different positions, which suggests that their T_c may be 16 K; caution should be exercised in interpreting the flux expulsion results due to other possible explanations, as detailed in Figure S2 (Supporting Information).

It is worth noting that both the sample-scale and cavity-plate depositions were performed using the same precursor concentration and reduction potential. However, the large-scale plate deposition had a six times smaller plating current density, likely due to the limited electrode size. To compensate for the reduced plating current, we extended the deposition duration to 29 h.

The T_c values obtained in this work (10.5– 13 K and possibly up to 16 K) approach the theoretical limit of ZrNb[33] and are close to those obtained under ultra-high pressures (28 GPa).[43] The 13 K T_c produced from the optimized condition is higher than the literature-reported values for ZrNb random alloys (11.5 K[16–18]) and sputtered ZrNb thin films (10.5 K[19–22]). The active phase determining T_c in the Zr-Nb diffusion couples (10.5 – 13.5 K) should be β-ZrNb. In contrast, the active phase in the electrochemical ZrNb(CO), consisting of multi-phases, requires open discussion.

2.3. Composition Analysis and Open Discussion on the Active Phase in ZrNb(CO)

The cross-sectional EDS elemental mapping under STEM (**Figure 4**a) and XPS depth profiling (Figure 4b) reveal the composition of Zr, Nb, C, and O as a function of depth. The sputter-assisted XPS elemental compositions provide the relative quantities of these four elements spatially averaged over an approximately 100 µm diameter probe. The local morphology with 3D features (Figure 4a) may affect this quantification, although XPS measurements at different sample locations show consistent depth profiles (Figure S9a, Supporting Information).

By decomposing different motifs under the Zr and Nb XPS spectra (for example, Figure 3d), we quantified the relative fractions of metallic-Zr versus ZrO_2 and metallic-Nb versus NbC, as shown in Figure S12 (Supporting Information). The surface layers are composed of ZrO_2. The film majority includes 30% metallic Zr versus 70% ZrO_2 and 65% metallic Nb versus 35% NbC. Note that the detection of ZrO_2 within the film may be from oxide precipitates or due to a residual signal induced by the surface roughness effect during ion sputtering. The nearly constant fractions over depth match the unaltered binding energy positions for Zr and Nb photoelectrons, despite their changing intensities at different depths (Figure S9d, Supporting Information).

The Zr doping concentration in β-ZrNb alloys is critical to their T_c's[33] and superheating fields.[34] We extract the Zr concentrations as a function of depth (Figure 4c) in the β-ZrNb part of ZrNb(CO), after excluding the ZrO_2 and NbC signals. The profile reveals an inhomogeneous distribution, with a concentration spike with a small depth of $\approx$ 10 nm, followed by a rapid decline reaching 10 –30 at.% Zr with a depth of $\approx$ 20 nm. Underneath these regions, the Zr concentrations remain < 10 at.% and extend to a depth of > 20 nm, consistent with the cross-sectional EDS depth profile (Figure 4a). These low-concentration Zr values agree with the maximum solubility of $\approx$ 9 at.% Zr in the equilibrium β-ZrNb at 600 ° C. These results also match the T_c calculations[33] predicting that the maximum T_c of 17.7 K occurs at a Zr concentration of 25 at.%, and the T_c at 9 at.% Zr is 16 K.

The question of whether the high T_c observed in this material system is determined by β-ZrNb or rocksalt NbC remains an open one. The literature reports that rocksalt NbC has T_c's of 9 – 11 K for bulk phases[68–71] and 8 – 11.5 K for thin films,[72,73] while rocksalt $Nb_xZr_{1-x}C$, or Zr doping in NbC, reduces the T_c.[74] However, DFT (density functional theory) simulations suggest that rocksalt and hexagonal NbC may have T_c's as high as 15.7[75] and 17.1 K,[76] respectively. Also, DFT simulations on the complex $NbC_{1-x}N_x$, or nitrogen doping in rocksalt NbC, predict T_c's ranging from 11.2 to 23.1 K,[77] suggesting that the effect of multiple light impurities on the T_c is not yet fully understood.

Our Zr-Nb diffusion couples containing β-ZrNb do not exhibit any detectable carbon signals, and these samples produce high T_c's close to those of ZrNb(CO). We argue that β-ZrNb is responsible for the observed T_c values above 11.5 K, although we cannot rule out the possibility of high-T_c NbC.

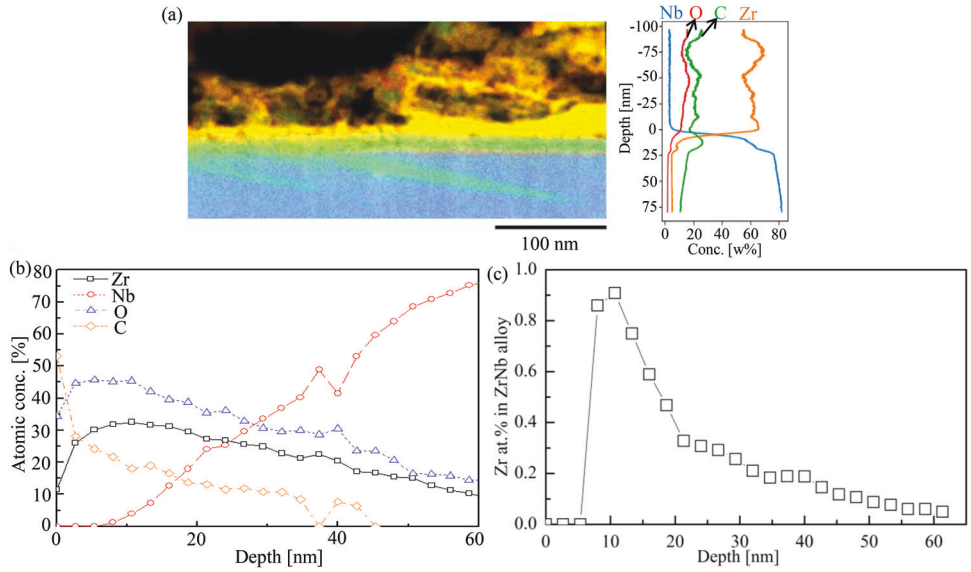

Figure 4. Composition profiles for the 10 h electrochemical ZrNb(CO). a) Cross-sectional STEM-EDS elemental map and local depth profile. b) XPS depth profiling. The probe size is ≈ 100 µm. c) Zr doping composition in β-ZrNb.

2.4. Superconducting RF Performance

We conducted a proof-of-concept RF demonstration of electrochemical ZrNb(CO) on the Cornell SRF sample test cavity[78,79] (see Experimental Section).

The temperature-dependent surface resistances of the thin ZrNb(CO) alloy were measured at 4.0 and 5.2 GHz with small RF field amplitudes of 2 ± 0.6 and 1 ± 0.3 mT, respectively, as the temperature was slowly decreased from 4.2 to 1.6 K over several hours. To indicate the temperature-dependent BCS resistance, we subtracted from the measured surface resistances its value at 1.6 K. **Figure 5**a presents these surface resistances as a function of temperature at 4.0 GHz and low amplitude fields (2 ± 0.6 mT). We found that the measured temperature-dependent BCS surface resistance trends toward lower values for ZrNb(CO) (pink circle) as compared to the reference Nb (cyan triangle), which is especially true at low fields and toward the higher end of the explored temperature range. This behavior was also observed at 5.2 GHz. Using a simple model, we estimated the surface resistance of a bi-layer consisting of a 50 nm film with a 16 K T_c over bulk niobium (Supporting Information). The predicted results (dashed lines) aligned with the observed reduction in surface resistance. While this model and specified parameters were not intended to be a rigorous explanation of the results, this analysis provides a simple check that such behavior is consistent with a thin film having an elevated T_c.

Low-temperature residual surface resistance with increasing field amplitude was measured for the ZrNb(CO) alloyed surface and the Nb reference (a baseline Nb that was later used for ZrNb(CO) deposition). The results at 1.6 K and 4.0 GHz are

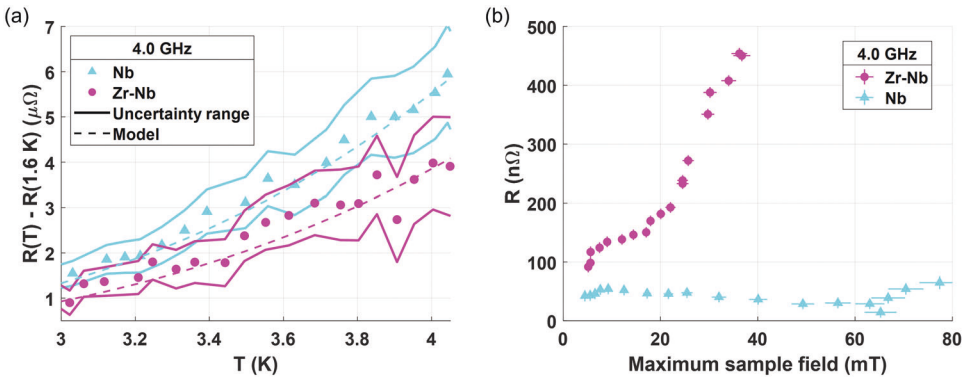

Figure 5. Superconducting RF performance of electrochemical ZrNb(CO). a) Measured surface resistances before (cyan triangles) and after (pink circles) the deposition of a ZrNb(CO) film onto a niobium substrate subtracted by its value at 1.6 K as a function of temperature at 4.0 GHz. R(1.6 K, 4.0 GHz) = 130 nΩ. The solid lines indicate the statistical uncertainty of the measurement. The cyan and pink colors indicate measurements of the niobium substrate before and after the growth of the ZrNb(CO) alloy. The dashed lines are model predictions from Equation (1) in Supporting Information. b) Measured total surface resistances at 1.6 K and 4.0 GHz comparing the field-dependence before (cyan triangles) and after (pink circles) the deposition of a ZrNb(CO) film onto a niobium substrate. The highest field reported for each set corresponds to the maximum value before a quench event, above which the superconducting properties are lost.

shown in Figure 5b. The ZrNb(CO) residual surface resistance was found to rapidly increase with input power before reaching its quench field, that is, the maximum RF magnetic field for which a flux-free Meissner state can exist. The quench fields were found to decrease from ≈ 80 mT at 4.0 GHz and ≈ 60 mT at 5.2 GHz with the original Nb substrate to ≈ 35 mT for both frequencies after the addition of the ZrNb(CO) film. A curious feature of the ZrNb(CO) alloy surface resistance is an apparent independence on frequency, at least for the two studied here. This is an unusual behavior that is in contrast to the baseline measurement of the niobium substrate prior to the ZrNb(CO) growth.

3. Conclusion

In summary, we have observed promising characteristics of electrochemically deposited ZrNb(CO) thin films that are desirable for applications ranging from particle accelerators to quantum devices. The performance metrics include (i) generation of β-ZrNb, (ii) avoidance of low-T_c hcp Zr, (iii) high T_c (at least 13 K) approaching the theoretical limit, and (iv) mild reduction of BCS resistance. This reduction could be more significant if the thickness of the ZrNb(CO) film were much larger than its penetration depth. This work marks the first step in developing electrochemical ZrNb(CO) and β-ZrNb for practical superconducting RF applications.

4. Experimental Section

Electrochemical Synthesis: Thick Nb (3mm, RRR > 300) substrates were electropolished via 9 H_2SO_4 : 1 HF with 100 µm removal, and they were cleaned by 2% HF before any deposition. The deposition was performed in an inert gas glovebox with O_2 and H_2O levels below 0.5 ppm. ZrF_4 and LiF were dissolved in the ionic liquid 1-Butyl-1-methylpyrrolidinium bis(trifluoromethylsulfonyl)imide at different concentrations (0.48 – 1.24 M ZrF_4 and 0.98 – 4.8 times LiF addition). Clear solutions of light-yellow color were obtained upon > 170 ° C heating, stirring, and standing, whereas the color turned brown during deposition. Chemicals were purchased from Krackeler Scientific, Inc., Alfa Aesar, and MilliporeSigma. A three-electrode electrochemical deposition system was employed, with Pt counter and quasi-reference wire electrodes. Electrochemical analysis was carried out using Princeton Applied Research VersaSTAT 3-500. Cyclic voltammetries were measured at scan rates of 10 – 50 mV s^{-1} to identify reduction potentials, and the temperature was varied from 30 to 200 ° C using a hotplate with feedback control. A potentiostat controlled the deposition, and the deposition time ranged from 2 to 10 h. After deposition, samples were cleaned with methanol, dried, and sealed in cleanroom plastic bags within the glovebox.

Post Annealing and Processing: The electrochemically synthesized samples were annealed in a Lindberg tube furnace at 600 °C for 10 h under 2×10^{-7} torr vacuum.

To identify the optimum annealing conditions, one initially investigated phase changes and diffusion properties using evaporated Zr-Nb diffusion couples. A Zr target was evaporated via e-beam on the electropolished bulk Nb surface at a 0.1 Å s^{-1} deposition rate under $1.3 - 1.8 \times 10^{-6}$ torr base pressure. These films were readily oxidized (Figure S14, Supporting Information), while ZrO_x/ZrNb/Nb structures were formed after annealing, which matches the observation of ZrNb interfacial alloys for oxidized-Zr/Nb thin films in literature.[66] Films of 20 and 40 nm thicknesses were annealed under 2×10^{-7} torr vacuum at 600 and 1000 ° C for 20 min – 10 h. One intended to design quenching and diffusion-dominated aging treatments through these annealing conditions. The heating rate was 5 ° C min^{-1}, and furnace cooling was used with average cooling rates of 10 ° C min^{-1} at 1000 ° C and 3 ° C min^{-1} at 600 ° C. After thermal annealing, samples were etched in 2% HF for 30 min to remove the surface ZrO_2 layer.

Structural and Elemental Characterization: A Zeiss Gemini scanning electron microscope (SEM) equipped with an in-lens detector under low voltage regimes (1 – 5 kV) was used to evaluate surface morphology and uniformity. Cross-sections of the surface layers were imaged by FEI F20 and Thermo-Fisher Scientific Kraken scanning transmission electron microscopes (STEM) after specimen preparation using a Thermo Fisher Helios G4 UX Focused Ion Beam (FIB). Elemental information was obtained by X-ray photoelectron spectroscopy (SSX-100 XPS) depth profiling and by energy dispersive X-ray spectroscopy (EDS) under STEM and SEM. The ion sputter rate for depth profiling was measured using a standard gold film, and this value was further calibrated by comparing the sputter yields simulated from the SRIM software (Figure S13, Supporting Information).[80] Phase information was determined by a high-resolution Rigaku SmartLab X-ray diffractometer (XRD) and local electron diffraction under STEM. The XRD step size was 0.0012°, and the scan rate was 1.44 ° min^{-1}. Note that attempt was made to minimize the samples' exposure to the atmosphere, for example, using a vacuum puck or in situ sample sealing, during transport from the glovebox to high or ultra-high vacuum techniques; still, short periods of exposure cannot be avoided.

Superconducting Property and RF Performance: The sample T_c was determined by temperature-dependent resistivity measurement conducted using a Quantum Design Physical Property Measurement System (PPMS) in the AC transport mode. Prior to the measurement, the sample surface was wedge-bonded to the sample puck using four 25 µm aluminum wires (West Bond 747630E Wire Bonder).

The flux expulsion test was also used to indicate T_c by detecting changes in the magnetic fields surrounding the sample as it was warmed up from liquid-helium temperatures. When a superconductor transitions from the superconducting state to the normal conducting state, previously expelled magnetic flux re-enters the superconductor, resulting in an abrupt change in the magnetic fields in its vicinity, as depicted in Figure S1 (Supporting Information). To conduct the tests, three flux gate magnetometers were attached to the back side of the Cornell sample test plate[78,79] to monitor the magnetic fields while the sample was slowly warmed up at a rate of ≈ 0.3 K min^{-1}. Each flux gate was oriented to measure the magnetic field along the axis normal to the sample surface, which was the dominant component of the fields in the cryostat, shielded to ambient values from ≈ 1 to ≈ 10 mG. The flux gates were positioned ≈ 2.5 cm from the sample edge, arranged in the shape of a triangle. The tests were repeated twice, and further details are included in Supporting Information.

To evaluate the RF performance of ZrNb(CO), one scaledup the electrochemical and annealing process to a 12.7 cm diameter Nb plate that was fitted for the Cornell SRF sample test cavity.[78,79] The cavity plate deposition used the same precursor concentration and reduction potential as the sample-scale deposition, but with a reduced plating current density due to the limited electrode size. To compensate, the deposition time to 29 h was extended.

The surface resistances and quench fields of the plate were measured with a thin surface layer of the ZrNb(CO) alloy at temperatures ranging from 1.6 to 4.2 K using the sample test cavity. This modified cylindrical cavity operates with 4.0 GHz TE_{011}-like and 5.2 GHz TE_{012}-like modes. The sample plate was attached to the host structure as an end plate to the cylindrical opening, ensuring that the field on the sample was nearly identical for both modes of operation. The host structure geometry is designed to focus the surface fields on the location of the sample plate, allowing fields up to 100 mT to be reached on the sample surface. The surface resistance of the sample plate was determined using a calibrated quality-factor measurement, with errors occurring when a sample has surface resistance comparable to that of the Nb host structure. For more information about this measurement setup and uncertainty analysis, see Ref. [79]

Supporting Information

Supporting Information is available from the Wiley Online Library or from the author.

Acknowledgements

Z.S. and T.O. contributed equally to this work. This work was supported by the U.S. National Science Foundation under Award PHY-1549132, the Center for Bright Beams. This work made use of the Cornell Center for Materials Research Shared Facilities which are supported through the NSF MRSEC program (DMR-1719875), and was performed in part at the Cornell NanoScale Facility, an NNCI member supported by NSF Grant NNCI-2025233. Z.S. thanks P. D. Bishop, A. Holic, J. Sears, G. Kulina, H. G. Conklin, and T. M. Gruber for helping with sample preparation and electrochemical system installation.

Conflict of Interest

A provisional patent related to this research is filed by Cornell University.

Author Contributions

Z.S. developed the methodology, conducted experiments on material growth, processing, optimization, characterization, and superconductivity measurements, and wrote the manuscript. T.O. conducted experiments and analyses on RF evaluation and flux expulsion test, and wrote the relevant section. Z.B. conducted experiments on cross-sectional STEM/EDS imaging and electron diffraction. D.K.D. assisted with XPS measurements, and K.H. assisted with part of the heat treatments. M.O.T., R.H., B.F., A.C.H., N.S., T.A.A., M.K.T., D.A.M., and M.U.L. provided valuable advice to design experiments and to understand results, mainly through the collaboration of the Center for Bright Beams. Z.S., T.O., Z.B., D.K.D., K.H., M.O.T., D.A.M., and M.U.L. further revised the manuscript. M.U.L. and D.A.M. acquired funding for the work and supervised this work.

Data Availability Statement

The data that support the findings of this study are available from the corresponding author upon reasonable request.

Keywords

critical temperature, electrochemical synthesis, phase transformations, radio-frequency superconductors, thin films

Received: March 3, 2023
Revised: May 9, 2023
Published online: June 21, 2023

[1] N. Huang, H. Deng, B. Liu, D. Wang, Z. Zhao, *Innovation* **2021**, *2*, 100097.
[2] B. W. J. McNeil, N. R. Thompson, *Nat. Photonics* **2010**, *4*, 814.
[3] P. G. O'Shea, H. P. Freund, *Science* **2001**, *292*, 1853.
[4] W. Decking, S. Abeghyan, P. Abramian, A. Abramsky, A. Aguirre, C. Albrecht, P. Alou, M. Altarelli, P. Altmann, K. Amyan, V. Anashin, E. Apostolov, K. Appel, D. Auguste, V. Ayvazyan, S. Baark, F. Babies, N. Baboi, P. Bak, V. Balandin, R. Baldinger, B. Baranasic, S. Barbanotti, O. Belikov, V. Belokurov, L. Belova, V. Belyakov, S. Berry, M. Bertucci, B. Beutner, et al., *Nat. Photonics* **2020**, *14*, 391.
[5] E. Prat, R. Abela, M. Aiba, A. Alarcon, J. Alex, Y. Arbelo, C. Arrell, V. Arsov, C. Bacellar, C. Beard, P. Beaud, S. Bettoni, R. Biffiger, M. Bopp, H.-H. Braun, M. Calvi, A. Cassar, T. Celcer, M. Chergui, P. Chevtsov, C. Cirelli, A. Citterio, P. Craievich, M. C. Divall, A. Dax, M. Dehler, Y. Deng, A. Dietrich, P. Dijkstal, R. Dinapoli, et al., *Nat. Photonics* **2020**, *14*, 748.
[6] V. Shiltsev, F. Zimmermann, *Rev. Mod. Phys.* **2021**, *93*, 015006.
[7] C. E. Reece, *Phys. Rev. Accel. Beams* **2016**, *19*, 124801.
[8] R. V. de Water, presented at 2022 North American Particle Accelerator Conf., Albuquerque, New Mexico **2022**.
[9] W. E. King, Geoffrey H. Campbell, Alan Frank, Bryan Reed, John F. Schmerge, Bradley J. Siwick, Brent C. Stuart, Peter M. Weber, *J. Appl. Phys.* **2005**, *97*, 111101.
[10] E. J. Jaeschke, S. Khan, J. R. Schneider, J. B. Hastings, in *Synchrotron Light Sources and Free-Electron Lasers: Accelerator Physics, Instrumentation and Science Applications*, Springer, Cham **2020**.
[11] W. Ehrfeld, A. Schmidt, *J. Vac. Sci. Technol., B: Microelectron. Nanometer Struct.–Process., Meas., Phenom.* **1998**, *16*, 3526.
[12] A. Blais, A. L. Grimsmo, S. M. Girvin, A. Wallraff, *Rev. Mod. Phys.* **2021**, *93*, 025005.
[13] A. Romanenko, R. Pilipenko, S. Zorzetti, D. Frolov, M. Awida, S. Belomestnykh, S. Posen, A. Grassellino, *Phys. Rev. Appl.* **2020**, *13*, 034032.
[14] M. H. Devoret, R. J. Schoelkopf, *Science* **2013**, *339*, 1169.
[15] A. Gurevich, *Nat. Mater.* **2011**, *10*, 255.
[16] J. M. Corsan, I. Williams, J. A. Catterall, A. J. Cook, *J. Less-Common Metals* **1968**, *15*, 437.
[17] J. K. Hulm, R. D. Blaugher, *Phys. Rev.* **1961**, *123*, 1569.
[18] S. Narasimhan, R. Taggart, D. H. Polonis, *J. Nucl. Mater.* **1972**, *43*, 258.
[19] A. Cavalleri, F. Giacomozzi, L. Guzman, P. M. Ossi, *J. Phys.: Condens. Matter.* **1989**, *1*, 6685.
[20] W. P. Lowe, T. H. Geballe, *Phys. Rev. B* **1984**, *29*, 4961.
[21] P. Koorevaar, W. Maj, P. H. Kes, J. Aarts, *Phys. Rev. B* **1993**, *47*, 934.
[22] U. Gambardella, D. Di Gioacchino, V. Boffa, G. Paterno, S. Barbanera, F. Murtas, *IEEE Trans. Appl. Supercond.* **1993**, *3*, 1253.
[23] S. Posen, M. Liepe, D. L. Hall, *Appl. Phys. Lett.* **2015**, *106*, 082601.
[24] T. Oseroff, M. Liepe, Z. Sun, presented at *Proc. 19th Int. Conf. RF Supercond.*, Dresden, Germany **2019**.
[25] Z. Sun, G. Gaitan, M. Ge, K. Howard, M. U. Liepe, R. D. Porter, T. Oseroff, presented at *Proc. 20th Int. Conf. RF Superconductivity*, Lansing, MI, USA **2021**.
[26] M. C. Burton, M. R. Beebe, K. Yang, R. A. Lukaszew, A.-M. Valente-Feliciano, C. Reece, *J. Vac. Sci. Technol., A* **2016**, *34*, 021518.
[27] K. Howard, M. Liepe, Z. Sun, presented at *Proc. 20th Int. Conf. RF Superconductivity*, Lansing, MI, USA **2021**.
[28] A. Grassellino, A Romanenko, Y. Trenikhina, M. Checchin, M. Martinello, O. S. Melnychuk, S. Chandrasekaran, D. A. Sergatskov, S. Posen, A. C. Crawford1, S. Aderhold, D. Bice, *Supercond. Sci. Technol.* **2017**, *30*, 9.
[29] S. Posen, J. Lee, D. N. Seidman, A. Romanenko, B. Tennis, O. S. Melnychuk, D. A. Sergatskov, *Supercond. Sci. Technol.* **2021**, *34*, 025007.
[30] J. Lee, S. Posen, Z. Mao, Y. Trenikhina, K. He, D. L. Hall, M. Liepe, D. N. Seidman, *Supercond. Sci. Technol.* **2018**, *32*, 024001.
[31] A. Pack, J. Carlson, S. Wadsworth, M. K. Transtrum, *Phys. Rev. B* **2020**, *101*, 144504.
[32] Z. Sun, Z. Baraissov, L. Shpani, R. D. Porter, Y.-T. Shao, T. Oseroff, M. O. Thompson, D. A. Muller, M. U. Liepe, *arXiv.2302.02054*, **2023**
[33] N. Sitaraman, Z. Sun, B. Francis, A. C. Hire, T. Oseroff, Z. Baraissov, T. A. Arias, R. Hennig, M. U. Liepe, D. A. Muller, M. K. Transtrum, *arXiv.2208.10678*, **2022**.
[34] B. Francis, M. Transtrum, Y. Quan, A. Hire, R. Hennig, M. Kelley, N. Sitaraman, T. Arias, *APS March Meeting Abstracts* **2022**, *2022*, B57.
[35] M. Tinkham, in *Introduction to Superconductivity*, Dover Publications, Mineola, NY, USA **1996**.
[36] K. Choo, Y. H. Kang, S. I. Pyun, V. F. Urbanic, *J. Nucl. Mater.* **1994**, *209*, 226.
[37] G. J. Cuello, A. F. Guillermet, G. B. Grad, R. E. Mayer, J. R. Granada, *J. Nucl. Mater.* **1995**, *218*, 236.

[38] G. Aurelio, A. Fernández Guillermet, G. J. Cuello, J. Campo, *Metall. Mater. Trans. A* **2003**, *34*, 2771.
[39] S. Banerjee, R. Krishnan, *Acta Metall.* **1971**, *19*, 1317.
[40] K. Holm, J. D. Embury, G. R. Purdy, *Acta Metall.* **1977**, *25*, 1191.
[41] H. L. Yang, Y. Matsukawa, S. Kano, Z. G. Duan, K. Murakami, H. Abe, *J. Nucl. Mater.* **2016**, *481*, 117.
[42] R. Kondo, N. Nomura, Suyalatu, Y. Tsutsumi, H. Doi, T. Hanawa, *Acta Biomater.* **2011**, *7*, 4278.
[43] H. Kawamura, J. Wittig, B. Bireckoven, W. Buckel, *Phys. B+C* **1984**, *126*, 485.
[44] B. T. Wang, P. Zhang, H. Liu, W.-D. Li, *J. Appl. Phys.* **2011**, *109*, 063514.
[45] H. Okamoto, *J. Phase Equilib.* **1992**, *13*, 577.
[46] Y. Liu, L. Zhang, T. Pan, D. Yu, Y. Ge, *Calphad* **2008**, *32*, 455.
[47] R. F. Hehemann, *Canadian J. Metall. Mater. Sci.* **1972**, *11*, 201.
[48] G. Aurelio, A. F. Guillermet, G. J. Cuello, J. Campo, *Journal of Nuclear Materials* **2005**, *341*, 1.
[49] M. Zhang, F. Zhang, Z. Yang, Y. Li, L. Qu, H. Zhen, *J. Alloys Compd* **2015**, *651*, 316.
[50] R. F. Hehemann, S. T. Zegler, *Trans. AIME* **1966**, *236*, 1594.
[51] G. B. Thompson, R. Banerjee, S. A. Dregia, H. L. Fraser, *Acta Mater.* **2002**, *51*, 5285.
[52] Y. Zhao, H. Li, Y. Huang, *J. Alloys Compd.* **2021**, *862*, 158029.
[53] D. Quaranta, L. Massot, M. Gibilaro, E. Mendes, J. Serp, P. Chamelot, *Electrochimica Acta* **2018**, *265*, 586.
[54] A. Girginov, T. Z. Tzvetkoff, M. Bojinov, *J. Appl. Electrochem.* **1995**, *25*, 993.
[55] H. Groult, A. Barhoun, H. E. Ghallali, S. Borensztjan, F. Lantelme, *J. Electrochem. Soc.* **2008**, *155*, E19.
[56] L. P. Polyakova, P. T. Stangrit, *Electrochimica Acta.* **1982**, *27*, 1641.
[57] C. Guang-Sen, M. Okido, T. Oki, *J. Appl. Electrochem.* **1990**, *20*, 77.
[58] B.-L. Yao, S. Senderoff, *J. Electrochem. Soc.* **2018**, *165*, D6.
[59] F. Basile, E. Chassaing, G. Lorthioir, *J. Appl. Electrochem.* **1981**, *11*, 645.
[60] R. Baboian, D. L. Hill, R. A. Bailey, *J. Electrochem. Soc.* **1965**, *112*, 1221.
[61] G. W. Mellors, S. Senderoff, *J. Electrochem. Soc.* **1966**, *113*, 60.
[62] G. J. Kipouros, S. N. Flengas, *J. Electrochem. Soc.* **1985**, *132*, 1087.
[63] M. A. Steinberg, M. E. Sibert, E. Wainer, *J. Electrochem. Soc.* **1954**, *101*, 63.
[64] G. M. Martinez, D. E. Couch, *Metall. Mater. Trans. B* **1972**, *3*, 575.
[65] F. P. Lin, A. Gurevich, *Phys. Rev. B* **2012**, *85*, 054513.
[66] Y. S. Li, K. C. Wong, P. C. Wong, K. A. R. Mitchell, *Appl. Surf. Sci.* **1996**, *103*, 389.
[67] A. Jain, S. P. Ong, G. Hautier, W. Chen, W. D. Richards, S. Dacek, S. Cholia, D. Gunter, D. Skinner, G. Ceder, K. A. Persson, *APL Mater.* **2013**, *1*, 011002.
[68] T. Shang, J. Z. Zhao, D. J. Gawryluk, M. Shi, M. Medarde, E. Pomjakushina, T. Shiroka, *Phys. Rev. B* **2020**, *101*, 214518.
[69] D. Yan, D. Geng, Q. Gao, Z. Cui, C. Yi, Y. Feng, C. Song, H. Luo, M. Yang, M. Arita, S. Kumar, E. F. Schwier, K. Shimada, L. Zhao, K. Wu, H. Weng, L. Chen, X. J. Zhou, Z. Wang, Y. Shi, B. Feng, *Phys. Rev. B* **2020**, *102*, 205117.
[70] L. E. Toth, V. F. Zackay, M. Wells, J. Olson, E. R. Parker, *Acta Metal.* **1965**, *13*, 379.
[71] N. K. Karn, M. M. Sharma, P. Sharma, G. Gurjar, S. Patnaik, V. P. S. Awana, *J. Supercond. Novel Magn.* **2021**, *34*, 2717.
[72] O. Meyer, G. Linker, B. Kraeft, *Thin Solid Films* **1973**, *19*, 217.
[73] G. Zou, Hongmei Luo, Yingying Zhang, Jie Xiong, Qiangmin Wei, Mujin Zhuo, Junyi Zhai, Haiyan Wang, Darrick Williams, Nan Li, Eve Bauer, Xinghang Zhang, Thomas M. McCleskey, Yanrong Li, Anthony K. Burrella, Q. X. Jia, *Chem. Comm.* **2010**, *46*, 7837.
[74] L. E. Toth, C. P. Wang, G. M. Yen, *Acta Metall.* **1966**, *14*, 1403.
[75] E. G. Maksimov, M. V. Magnitskaya, S. V. Ebert, S. Yu. Savrasov, *J. Exp. Theor. Phys.* **2004**, *80*, 548.
[76] X. Li, J.-G. Si, L.-T. Shi, P.-F. Liu, P. Zhangde B.-T. Wang, *Phys. Chem. Chem. Phys.* **2022**, *24*, 18419.
[77] S. Blackburn, M. Côté, S. G. Louie, M. L. Cohen, *Phys. Rev. B* **2011**, *84*, 104506.
[78] T. Oseroff, M. Liepe, Z. Sun, presented at *Proc. 2021 Int. Conf. on RF Superconductivity*, Lansing, MI, USA **2021**.
[79] T. Oseroff, Ph.D. Thesis, Cornell University, **2022**.
[80] J. F. Ziegler, *Nucl. Instrum. Methods Phys. Res., Sect. B* **2004**, *219-220*, 1027.